INSTITUTE OF PHYSICS PUBLISHING and INTERNATIONAL ATOMIC ENERGY AGENCY NUCLEAR FUSION

Nucl. Fusion **46** (2006) 403–411 doi:10.1088/0029-5515/46/4/001

Theory-based model for the pedestal, edge stability and ELMs in tokamaks

A.Y. Pankin[1], G. Bateman[2], D.P. Brennan[3], D.D. Schnack[1], P.B. Snyder[4], I. Voitsekhovitch[5], A.H. Kritz[2], G. Janeschitz[6], S. Kruger[7], T. Onjun[8], G.W. Pacher[9] and H.D. Pacher[10]

[1] SAIC, 10260 Campus Point Dr., San Diego, CA 92121, USA
[2] Lehigh University, Bethlehem, PA 18015, USA
[3] MIT, Cambridge, MA 02139, USA
[4] General Atomics, San Diego, CA 92186, USA
[5] JET-UKAEA, Culham Science Centre, UK
[6] FZK-PL-Fusion, Karlsruhe, Germany
[7] Tech-X, Boulder, CO 80303, USA
[8] SIIT, Klong Luang, Pathumthani 12121, Thailand
[9] Hydro-Québec, Varennes, Québec, Canada
[10] INRS, Québec, Canada

Received 13 December 2004, accepted for publication 12 January 2006
Published 17 February 2006
Online at stacks.iop.org/NF/46/403

Abstract
An improved model for triggering edge localized mode (ELM) crashes is developed for use within integrated modelling simulations of the pedestal and ELM cycles at the edge of H-mode tokamak plasmas. The new model is developed by using the BALOO, DCON and ELITE ideal MHD stability codes to derive parametric expressions for the ELM triggering threshold. The whole toroidal mode number spectrum is studied with these codes. The DCON code applies to low mode numbers, while the BALOO code applies to only high mode numbers and the ELITE code applies to intermediate and high mode numbers. The variables used in the parametric stability expressions are the normalized pressure gradient and the parallel current density, which drive ballooning and peeling modes. Two equilibria motivated by DIII-D geometry with different plasma triangularities are studied. It is found that the stable region in the high triangularity discharge covers a much larger region of parameter space than the corresponding stability region in the low triangularity discharge. The new ELM trigger model is used together with a previously developed model for pedestal formation and ELM crashes in the ASTRA integrated modelling code to follow the time evolution of the temperature profiles during ELM cycles. The ELM frequencies obtained in the simulations of low and high triangularity discharges are observed to increase with increasing heating power. There is a transition from second stability to first ballooning mode stability as the heating power is increased in the high triangularity simulations. The results from the ideal MHD stability codes are compared with results from the resistive MHD stability code NIMROD.

PACS numbers: 52.35.Py, 52.55.Fa

(Some figures in this article are in colour only in the electronic version)

1. Introduction

During the development of integrated modelling of the core of tokamak plasmas, impressive agreement with experimental observations has been achieved using different transport models such as the multi-mode (MM), GLF23 and mixed Bohm/gyro-Bohm (or JET) transport models [1–3]. Models are now being developed to simulate the physics of the edge of tokamak plasmas. Wide ranges of time and length scales need to be considered and many different elements of physics are involved at the plasma edge. The physics topics that are critically important for the plasma edge are the transition from low- to high- confinement regime (L–H transition), H-mode pedestal build up, anomalous and neoclassical transport at the plasma edge, role of the $\vec{E}_r \times \vec{B}$ flow shear and triggering and dynamics of the edge localized modes (ELMs). None of these problems is completely understood. Numerous theories, hypotheses and ideas are being considered for each of these problems. One of the effective ways to test ideas for physics models is to combine

them within an integrative modelling code and compare the simulation results with the experiments. Integrated modelling studies that self-consistently take into account the effects of the plasma edge have been developing during the last decade [4–8]. Some of these simulations are rather comprehensive and take into account MHD equilibrium, turbulent anomalous and collisional neoclassical radial transport, neutral gas transport, atomic and molecular physics and plasma–wall interactions.

A new model for the H-mode pedestal and ELMs has been recently developed by Pankin *et al* [8]. The model predicts the height, width and shape of the H-mode pedestal as well as the frequency of the ELMs. The model for the H-mode pedestal in tokamak plasmas is based on flow shear reduction of anomalous transport. The formation of the pedestal and the L–H transition in this model are the direct result of $\vec{E}_r \times \vec{B}$ flow shear suppression of transport.

Edge localized modes (ELMs) are among the determinant factors at the plasma edge that affect the whole plasma profiles, since up to 10% of the plasma energy can be removed by a single ELM crash. An ELM crash can be initiated either by a pressure driven ballooning instability or by a current driven peeling instability [9, 10]. Two mechanisms for triggering of ELMs have been considered in the model for ELMs [8]. ELMs are triggered by ballooning modes if the pressure gradient exceeds the ballooning limit or by peeling modes if the edge current density exceeds the peeling mode criterion. The model for the pedestal and ELMs has been used in a predictive integrated modelling code to follow the time evolution of tokamak discharges from L-mode through the transition from L-mode to H-mode, with the formation of the H-mode pedestal, and, subsequently, the triggering of ELMs.

The model for the H-mode pedestal and ELMs [8] is advanced in this paper. The ELM triggering conditions are studied with the MHD stability codes BALOO [11], DCON [12] and ELITE [13]. These MHD instability codes are used to compute the combined peeling–ballooning threshold, which are then used to derive fitting expressions that are included in the model. Using these computed MHD instability criteria produces a more accurate ELM trigger model. In particular, the ballooning criterion implemented previously is valid only in the first ballooning stability limit, while many recent DIII-D discharges operate in the second stability domain [14]. In the previous study [8], a simplified expression for the first ballooning stability limit was used, and the second ballooning stability limit was not implemented. Also, for the peeling stability criteria, a simplified analytical formula, that was valid in only a limited parameter range was used. The improved stability criterion model is implemented and used in the integrated modelling code ASTRA [15]. Cases with low and high triangularity are considered.

The intent of this paper is to show the development of a new model for parametrization of the MHD stability condition used to trigger ELMs, to describe the implementation of this model in the ASTRA code and to illustrate its use by carrying out simulations of low and high triangularity plasmas. In the stability analysis, it is found that the peeling and ballooning stability properties of high and low triangularity plasmas differ significantly. In order to illustrate the effect of MHD stability on the ELM characteristics, simulations with the integrated code, ASTRA, are carried out. These simulations are not meant to match precisely experimental conditions. Although the equilibria that we use are based on DIII-D geometry (i.e. major radius, minor radius, elongation and triangularity) and the density and heating profiles are taken from a low triangularity DIII-D discharge, there is no other connection to experimental data. Consequently, comparison between the simulations in this paper and experimental data is beyond the scope of the paper.

This paper is organized in the following manner. In section 2, a model for the H-mode pedestal and ELMs is introduced. The model is based on $\vec{E}_r \times \vec{B}$ flow shear suppression of anomalous thermal transport. Two ELM triggering mechanisms are considered: ELM crashes are caused either by ballooning mode instabilities or by peeling mode instabilities. Section 3 contains an MHD stability analysis of two cases, which are based on equilibria with high and low triangularity. The TOQ code is used to generate the equilibria, and the BALOO, DCON and ELITE codes are used to study the MHD stability at the plasma edge. The pedestal temperature, plasma density and bootstrap current are varied in a systematic manner to find a peeling–ballooning threshold. Fitting expressions for the threshold is implemented in the model for the H-mode pedestal and ELMs. The details of implementation and simulation results are reported in section 4. Discussion of the results and conclusions are presented in section 5.

2. Combined model for H-mode pedestal and ELM crashes

The model used in this paper for the H-mode pedestal and ELMs has been introduced in [8]. The H-mode pedestal formation is computed by suppression of the anomalous transport at the plasma edge. In order to take into account the fact that different instabilities are suppressed by the $\vec{E}_r \times \vec{B}$ flow shear at different rates, separate flow shear suppression functions $F_l^{(j)}$ are used. The contributions from the different instabilities together with the neoclassical thermal diffusivity, χ_{neo}, constitute the total ion and electron thermal diffusivity:

$$\chi_i = F_{\text{TGM}}^{(i)} \chi_{\text{TGM}}^{(i)} + F_{\text{RB}}^{(i)} \chi_{\text{RB}}^{(i)} + \chi_{\text{neo}}^{(i)}, \tag{1}$$

$$\chi_e = F_{\text{TGM}}^{(e)} \chi_{\text{TGM}}^{(e)} + F_{\text{RB}}^{(e)} \chi_{\text{RB}}^{(e)} + \chi_{\text{ETG}} + \chi_{\text{neo}}^{(e)}, \tag{2}$$

where

$$F_l^{(j)} = \frac{1}{1 + \alpha_l^{(j)} (\omega_{\text{ExB}} \tau_{lj})^2}, \quad l = (\text{TGM, RB}), \quad j = (\text{ions, electrons}), \tag{3}$$

and where $\chi_l^{(j)}$ is the anomalous thermal diffusivity without flow shear stabilization and τ_{lj} is the turbulence correlation time. The ITG and TEM thermal diffusivities, $\chi_{\text{TGM}}^{(j)}$, which are referred to as drift temperature gradient driven modes (TGM) in this paper, and the resistive ballooning diffusivities, $\chi_{\text{RB}}^{(j)}$, are computed with the MM transport model [16]. The ETG modes are not suppressed by the $\vec{E}_r \times \vec{B}$ flow shear in this model. The ETG contribution, χ_{ETG}, is computed with the Horton model [17]. Neoclassical thermal contributions, χ_{neo}, are not affected by the $\vec{E}_r \times \vec{B}$ flow shear and are computed using the NCLASS module [18].

The flow shear rate $\omega_{E\times B}$ is defined as

$$\omega_{E\times B} \equiv \left| \frac{RB_\theta}{B_\phi} \frac{\partial}{\partial r} \left(\frac{E_r}{RB_\theta} \right) \right|, \quad (4)$$

where B_θ and B_ϕ are poloidal and toroidal components of the magnetic field, R is the major radius and E_r is the radial component of electric field.

The simulations in this paper were carried out with a new version of the ASTRA code, version 6.0, compared with version 5.3 used in [8]. The equilibrium package used in the new version of the ASTRA code produces a q-profile and a radial profile of flux surface shapes that are more accurate. As a consequence, a recalibration of the flow shear coefficients was required. The flow shear part of the model is used to compute the H-mode pedestal formation. It remains unchanged relative to the model introduced in [8] except for an updated version of the model for neoclassical transport NCLASS and re-calibrated coefficients for the $\vec{E}_r \times \vec{B}$ flow shear suppression, $\alpha_l^{(j)}$. The remainder of the edge model is used to compute the trigger for ELM crashes and the consequences of each ELM crash. The changes of the edge temperature profiles resulting from each ELM crash and the width of the ELM crash are described in [8]. Plasma density profiles, which are taken from experimental data for a low triangularity DIII-D discharge, remain unchanged in these simulations. A full particle transport model would be important for an accurate determination of the pedestal formation and growth between ELM crashes. However, since the focus of this paper is on the effect of MHD stability, the density profile just prior to an ELM crash is adequate for the test of the MHD stability condition. It has been suggested, based on ideal MHD simulations [19], that the width of the ELM crash can be determined by the width of the most unstable mode. However, since a full-featured MHD code is not included in the ASTRA code, an empirical scaling is used to determine the width of the ELM crash [8] in this paper. The width of the ELM region is computed from an empirical expression for the plasma energy removed by an ELM crash [9, 20].

An ELM crash in this model can be triggered either by a pressure-driven ballooning instability or by a current-driven peeling instability [9, 10]. The combined effects of ballooning and peeling criteria are shown on a schematic diagram in figure 1 [9, 19]. The part of the curve to the left of point A in figure 1 represents the peeling mode stability criterion; the part of the curve to the right of point A represents the ballooning mode stability criterion. A simplified condition for the peeling and ballooning threshold has been used in the previous version of the edge model [8]. In particular, the peeling criterion has been defined by an approximate analytical expression given in [21]. The peeling mode criterion involves the Mercier coefficient, which is proportional to the pressure gradient, and the parallel component of the plasma current density. It reflects the fact that the peeling mode is destabilized by the parallel current and is stabilized by the plasma pressure gradient. This criterion for the peeling instability does not include a dependence on plasma shaping and does not account for the stabilizing effects of the vacuum region, except through an adjustable coefficient. The ballooning instability criterion used in the previous implementation of the model is valid only in the first ballooning stability limit. These limitations for the

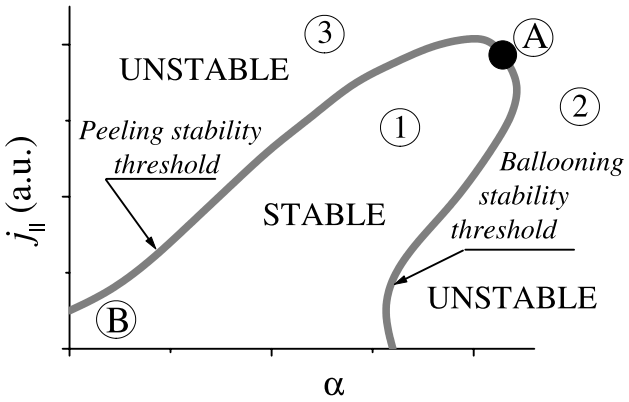

Figure 1. Schematic diagram of an ELM crash. The stable region ① separates two unstable regions ② and ③. In the region ②, the ELM crashes are caused by the ballooning instability; in the region ③, the ELM crashes are caused by the peeling instability. The ballooning–peeling threshold is shown as a function of the parallel component of current density, $j_\parallel$ and the normalized pressure gradient, α. In general, the parallel component of the plasma current density destabilizes the peeling mode and the pressure gradient stabilizes the peeling mode and destabilizes the ballooning mode.

peeling and ballooning criteria have the effect of narrowing the ranges of applicability of the model. In general, the peeling and ballooning threshold depends on many different parameters, which make them difficult to parametrize. An MHD stability analysis is carried out for the range of the normalized pressure gradient and plasma current density that are predicted in the ASTRA transport simulations, in order to derive an expression for the peeling–ballooning threshold as a function of these parameters. This parametric expression can be used to trigger ELM crashes in transport simulations. This approach is described in the next section of this paper in detail.

During each ELM crash, the bootstrap current density changes rapidly in response to the rapid changes in the edge temperature profiles. However, the local current density decreases more slowly due to inductive effects, since it is computed using a magnetic diffusion equation with a prescribed total plasma current, which automatically adjusts the loop voltage as needed. The current density in the pedestal is pushed into the plasma during a short time interval after each ELM crash. As the pedestal rebuilds during the rest of the ELM cycle, the increasing pressure gradient drives an increasingly large bootstrap current density which, in turn, drives an increasingly large current density in the pedestal.

3. Peeling–ballooning stability analysis

Two reference cases, which are based on two equilibria with different triangularity, motivated by DIII-D geometry, are considered in this paper. Plasmas with high triangularity, $\delta = 0.6$, and low triangularity, $\delta = 0.2$, are considered. Other plasma parameters are held fixed in the reference cases: the minor radius $a = 0.63$ m; major radius $R = 1.69$ m; toroidal magnetic field $B_T = 2.0$ T; plasma current $I = 1.54$ MA; elongation $\kappa = 1.78$; central plasma density $n_e(0) = 4.7 \times 10^{19}$ m^{-3} and central ion and electron temperatures $T_{e,i} = 4$ keV. The TOQ equilibrium code [11] is used to generate a set of equilibria that covers the range of transport simulations

for the plasma parameters given above. As long as the plasma geometry, toroidal magnetic field and total plasma current are fixed in the transport simulations, ELMs are controlled only by the pressure gradient and bootstrap current. The total current and the bootstrap current are computed in the TOQ code. The bootstrap current is obtained using the Sauter formula [22]:

$$\langle j_\parallel B\rangle = \sigma_{\rm neo}\langle E_\parallel B\rangle - I(\psi)p_e \times\left[\mathcal{L}_{31}\frac{p}{p_e}\frac{\partial \ln p}{\partial\psi} + \mathcal{L}_{32}\frac{\partial \ln T_e}{\partial\psi} + \mathcal{L}_{34}\lambda\frac{\partial \ln T_i}{\partial\psi}\right], \quad (5)$$

where $\sigma_{\rm neo}$ is the neoclassical resistivity, $I(\psi) = RB_\phi$, ψ is the normalized poloidal flux and $\mathcal{L}_{31}$, $\mathcal{L}_{32}$, $\mathcal{L}_{34}$ and λ are the bootstrap coefficients, which depend on the electron and ion collisionalities ν_{e*} and ν_{i*} and on the trapped fraction f_t.

In order to find the peeling–ballooning stability threshold, it is necessary to explore a range of parameter space for the current density while the shape of the current density profile is determined by the shape of the bootstrap current density. This exploration of parameter space is accomplished by introducing the scale factor, $C_{\rm boot}$, in the DCON code:

$$\hat{j}_\parallel = C_{\rm boot}\, j_\parallel. \quad (6)$$

The ballooning and peeling mode stability criteria depend upon the shapes of the pressure and current density profiles as well as their magnitudes. Consequently, the MHD stability calculations are carried out with profiles that represent the profiles obtained as the pedestal evolves in the ASTRA simulations. The density and temperature profiles are defined with the following polynomial dependences as in [23]:

$$n_e(\psi) = n_{\rm sep} + a_{n0}\left[\tanh\left(2\frac{1-\psi_{\rm mod}}{\Delta}\right) - \tanh\left(2\frac{\psi-\psi_{\rm mid}}{\Delta}\right)\right] + a_{n1}H\left(1-\frac{\psi}{\psi_{\rm ped}}\right) \times\left[1-\left(\frac{\psi}{\psi_{\rm ped}}\right)^{\alpha_{n1}}\right]^{\alpha_{n2}},$$

$$T_e(\psi) = T_{\rm sep} + a_{T0}\left[\tanh\left(2\frac{1-\psi_{\rm mod}}{\Delta}\right) - \tanh\left(2\frac{\psi-\psi_{\rm mid}}{\Delta}\right)\right] + a_{T1}H\left(1-\frac{\psi}{\psi_{\rm ped}}\right) \times\left[1-\left(\frac{\psi}{\psi_{\rm ped}}\right)^{\alpha_{T1}}\right]^{\alpha_{T2}},$$

where Δ is the pedestal width, H is the Heaviside step function, $n_{\rm sep}$ and $T_{\rm sep}$ are the electron density and temperature at separatrix, respectively, $\psi_{\rm ped} = 1-\Delta$ and $\psi_{\rm mid} = 1-\Delta/2$. The constants a_{n0}, a_{n1}, a_{T0} and a_{T1} are computed in TOQ to satisfy the values of the plasma density and temperature at the top of the pedestal and plasma centre. The parameters α_{n1}, α_{n2}, α_{T1} and α_{T2} control the shape of the electron density and temperature profiles in the plasma core. The profiles given by equation (7) resemble the experimentally measured profiles and were used in the peeling–ballooning ideal MHD stability analysis by Snyder *et al* [19,23]. The parameters that specify the profiles in the plasma core are kept the same for all scans: $\alpha_{n1} = \alpha_{n2} = \alpha_{T1} = 1.1$ and $\alpha_{T2} = 2$. Also, the shape of the electron density profile is kept unchanged in all scans; the electron density at the top of the pedestal is set to satisfy the dependence $n_{\rm ped} = 0.71\langle n_e\rangle$, which is a scaling obtained from a pedestal data base study [24].

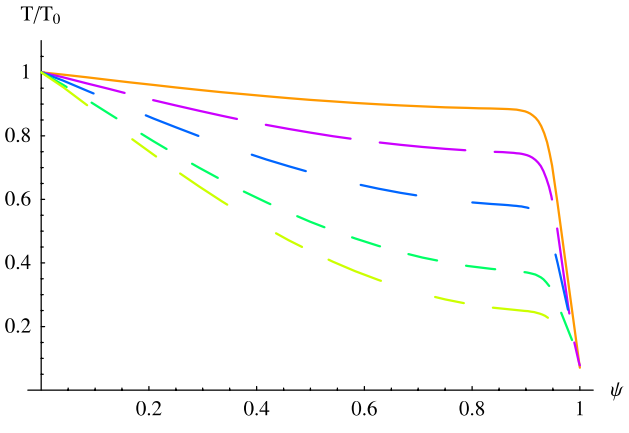

Figure 2. Temperature profiles that are used in the TOQ code to generate a set of equilibria for analysis with the ideal MHD stability codes. The central temperature is fixed and the temperature at the top of the pedestal is changed.

In the temperature scan, the central temperature is kept fixed, while the pedestal temperature is changed (see figure 2). Both the bootstrap current and pressure gradient are changed in the temperature scan. In the ASTRA transport simulations, the change in the bootstrap current results only from the change in the temperature gradient during an ELM cycle. In the ASTRA simulations, the density profile remains unchanged during the ELM cycle and remains unchanged from one simulation to the next.

The temperature scan also provides control of the normalized pressure gradient, α, which is defined in this study as

$$\alpha = -\frac{\mu_0}{2\pi^2}\frac{\partial p}{\partial\psi}\frac{\partial V}{\partial\psi}\left(\frac{V}{2\pi^2 R}\right)^{1/2}, \quad (7)$$

where V is the plasma volume and ψ is the poloidal flux.

In the reference equilibrium case, the central temperature is set to 4 keV and the central electron density is set to $4.7\times10^{19}\,{\rm m}^{-3}$. About 120 equilibria are generated for the high triangularity case and about 75 equilibria are generated for the low triangularity case by changing the TOQ parameters $T_{\rm ped}$ in the range from 250 to 3250 eV and $C_{\rm boot}$ in the range from 0.3 to 2.2. These ranges extend beyond what is normally observed in order to insure that the model covers the entire possible parameter range in the simulations. These equilibria are used in the BALOO, DCON and ELITE codes to validate the peeling–ballooning stability criteria in the limits of different toroidal mode numbers. The BALOO code [11] is an infinite mode number ballooning stability code developed at General Atomics. The ideal MHD DCON code is suitable for the stability analysis of low toroidal number ballooning and peeling modes, and the ELITE code works well for the analysis of intermediate and high mode numbers. Since these codes are complementary, they can be used together to compute the stability criteria. The BALOO and DCON codes are called routinely from the same script that is used for the equilibrium generated by the TOQ code. The stability of low toroidal mode numbers up to $n = 7$ are analysed with the DCON code. In addition, the DCON code has an option to check the

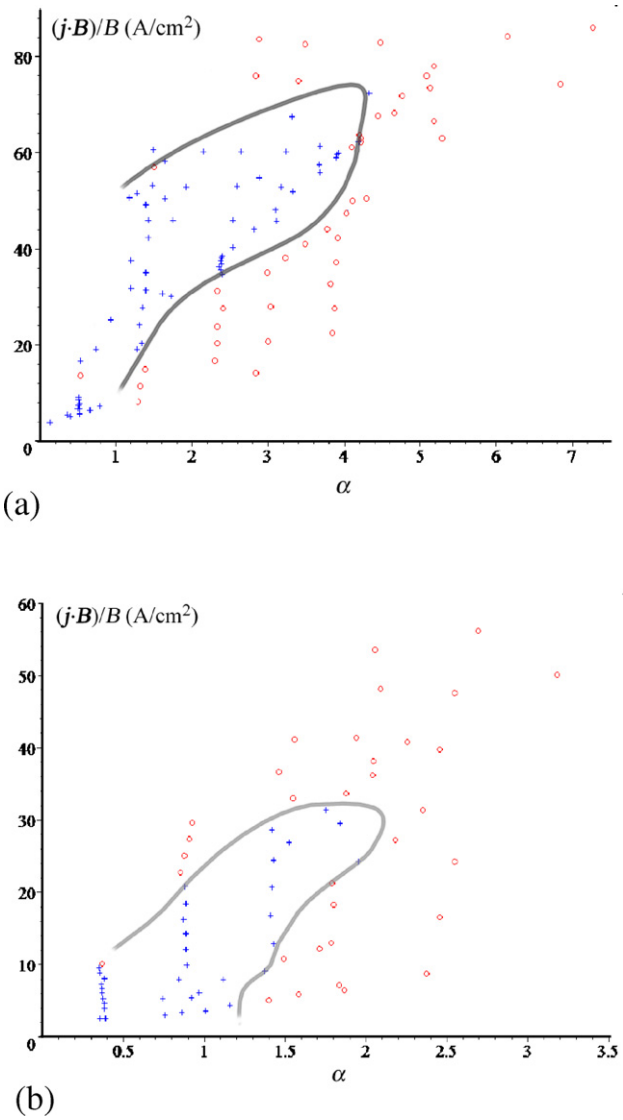

Figure 3. ELM stability diagrams for discharges with (*a*) high ($\delta = 0.6$) and (*b*) low ($\delta = 0.2$) triangularity. The solid curve separates stable and unstable regions. The '+' symbol on the diagrams corresponds to the cases that are tested with the MHD stability codes that appear to be stable; the 'o' symbol on the diagram corresponds to the cases that appear to be unstable. The normalized pressure gradient, α, and the parallel component of the current density, $\mathbf{j} \cdot \mathbf{B}/B$, are computed at the 97% flux surface.

stability of infinite n modes, which allows the results of DCON and BALOO to be cross-verified. The ELITE code is called for several equilibria that are close to the peeling–ballooning stability threshold.

The results of the stability analysis for high ($\delta = 0.6$) and low ($\delta = 0.2$) triangularity discharges are shown in figure 3. The solid curves in figure 3 separate the stable and unstable regions. The '+' symbols mark stable regions of parameter space while the 'o' symbols mark unstable regions. The high triangularity discharge has a larger stable region than the low triangularity discharge, which is consistent with experimental results and other MHD stability analyses [23]. In particular, the higher triangularity discharges have a larger second stability region, which is also consistent with the conclusion that higher

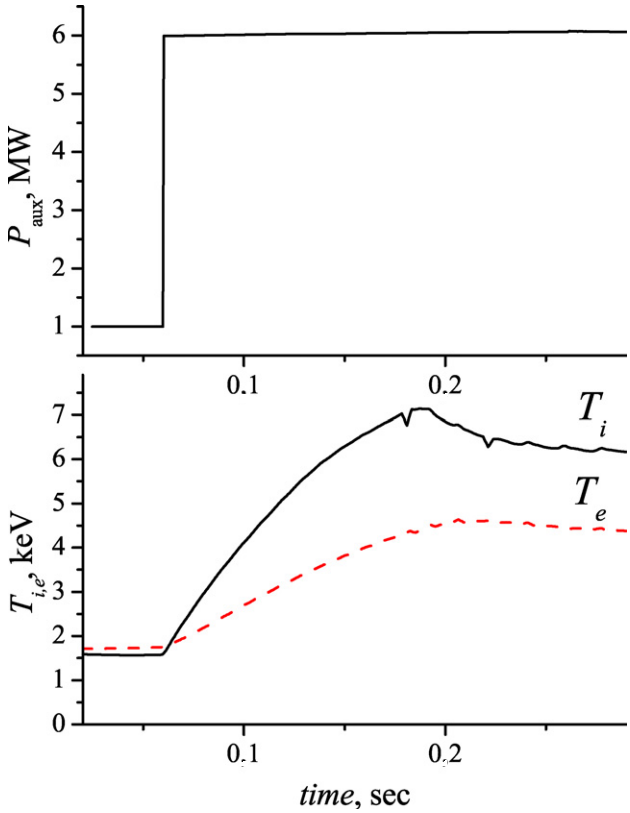

Figure 4. The NBI heating power absorbed by the ions and electrons as a function of time is shown in the top panel. The central electron and ion temperatures from ASTRA simulations are plotted as a function of time at the plasma centre in the bottom panel.

triangularity discharges can more easily access the second ballooning stability region of parameter space [6].

The peeling–ballooning stability threshold shown in figure 3 is parametrized using fifth order polynomials:

$$j_{\parallel}^{\mathrm{stab}} = \sum_{i=0}^{5} b_i \alpha^i, \tag{8}$$

where b_i are the parametrization coefficients. Each peeling–ballooning threshold is parametrized using two polynomials: one for the higher boundary (peeling threshold) and the other for the lower boundary (ballooning threshold). The polynomials for the peeling–ballooning threshold are implemented in the ASTRA transport code and used as the criteria to trigger ELM crashes in the transport simulations.

4. Results of integrated transport simulations

A reference scenario for ASTRA simulations is based on a typical high triangularity DIII-D geometry described in [25]. The parameters for this discharge are listed at the beginning of the previous section. In addition, the electron, ion and impurity density profiles, toroidal rotation velocity, Z_{eff}, the current density driven by the neutral beam injection (NBI) heating and the auxiliary heating power deposited to electrons and ions, which are obtained from an analysis simulation of experimental data, are prescribed and fixed in form. The experimental radial profile of the total current density is used

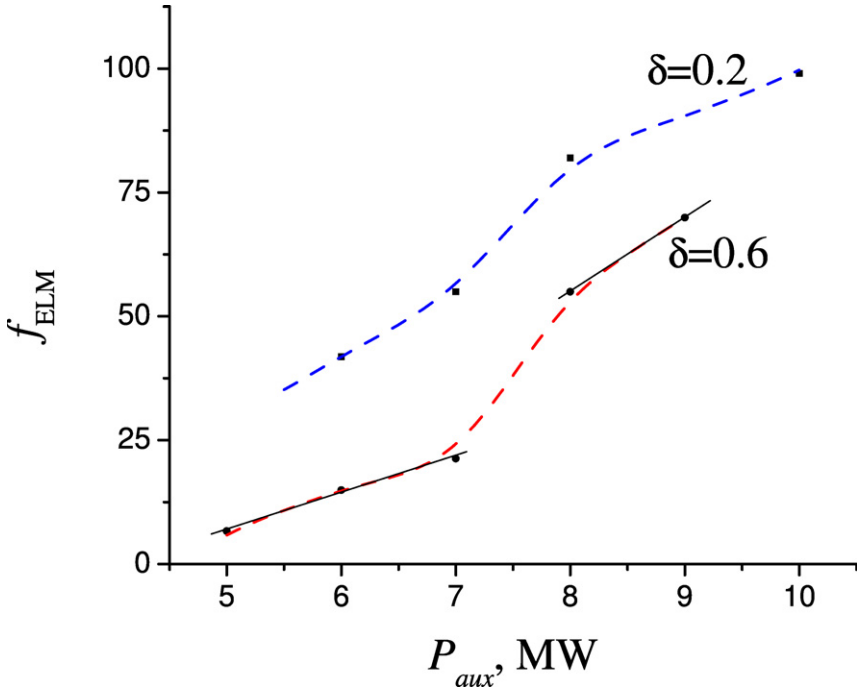

Figure 5. The frequency of ELM crashes as a function of the auxiliary heating power for discharges with low ($\delta = 0.2$) and high ($\delta = 0.6$) triangularities.

as an initial condition for the magnetic diffusion equation, which is solved in the ASTRA code. The ASTRA code does not use the equilibria computed with the TOQ code described in the previous section of the paper; instead, the ESC equilibrium module is called to follow the dynamically evolving equilibrium in the ASTRA code.

In the reference scenario, the NBI auxiliary heating power deposited to electrons and ions in the simulation is increased from 1 MW to approximately 6 MW at 0.06 s, as shown in figure 4. In the ASTRA simulation, the electron and ion temperatures are observed to increase after the heating power increases, and the transition from L- to H-mode is observed at about 0.07 s. An H-mode pedestal is formed at this time in both electron and ion temperature profiles. For both the lower and higher triangularity discharges, the auxiliary heating power after 0.06 s is varied from 3.5 to 7.0 MW in a series of simulations. The ELM frequencies as a function of auxiliary heating power for discharges with higher and lower triangularities are shown in figure 5. It can be seen that the ELM frequency increases with increasing heating power in the simulations.

In [8], two possible scenarios were discussed. In the first scenario, ELM crashes are triggered by the ballooning instability in the first ballooning stability limit. In the second scenario, an ELM crash triggered by a ballooning instability in the first ballooning stability limit is followed by a series of frequent ELM crashes triggered by a peeling instability. In the current study, a complete peeling–ballooning threshold is implemented and an additional scenario is observed in the simulations. For the higher triangularity discharge and higher auxiliary heating powers, a single ELM crash triggered by a ballooning instability in the second ballooning stability limit can be followed by a series of more frequent ELM crashes triggered by a ballooning instability in the first ballooning stability limit (see figures 6 and 7). The range of bootstrap current where the peeling and ballooning instabilities are stable is shown on the lower panels in figure 6. The critical values of bootstrap current are changing with time in accordance with the stability diagram shown in figure 3. Points A, B and C on the lower panels in figure 6 correspond to the first ELM cycle in the two ASTRA simulations with lower ($P_{\rm aux} = 6$ MW) and higher heating powers ($P_{\rm aux} = 8$ MW). The difference between the two cases is also demonstrated in figure 7 that shows an ELM cycle on the peeling–ballooning stability diagram. In both the cases of lower and higher heating powers, the first ELM crash (point A on figures 6 and 7) is caused by the ballooning instability in the second stability limit. The pedestal pressure and bootstrap current drop from point A to point B and then recover to point C (next ELM crash) in figure 7. In the case of lower heating power, the next ELM crash is also caused by the ballooning instability in the second stability limit; in the case of higher heating power, the next ELM crash is caused by the ballooning instability in the first stability limit. The difference in the two scenarios can be explained by the different rates of rebuilding of pedestal pressure and bootstrap current in the pedestal region. In general, access to the second stability region results in edge pressure gradients that reach higher levels. Because of this, the ELM crashes triggered by a ballooning instability in the first stability limit are more frequent than the ELM crashes triggered by a ballooning instability in the second stability limit. The change of ELM frequency level as a result of the transition from the second to the first ballooning stability for the high triangularity simulations is shown in figure 5. There is no transition from the second to the first stability as heating power is increased in the lower triangularity simulations. In the high triangularity ASTRA simulations, the discharges with low auxiliary heating (below 7 MW) have ELM crashes that

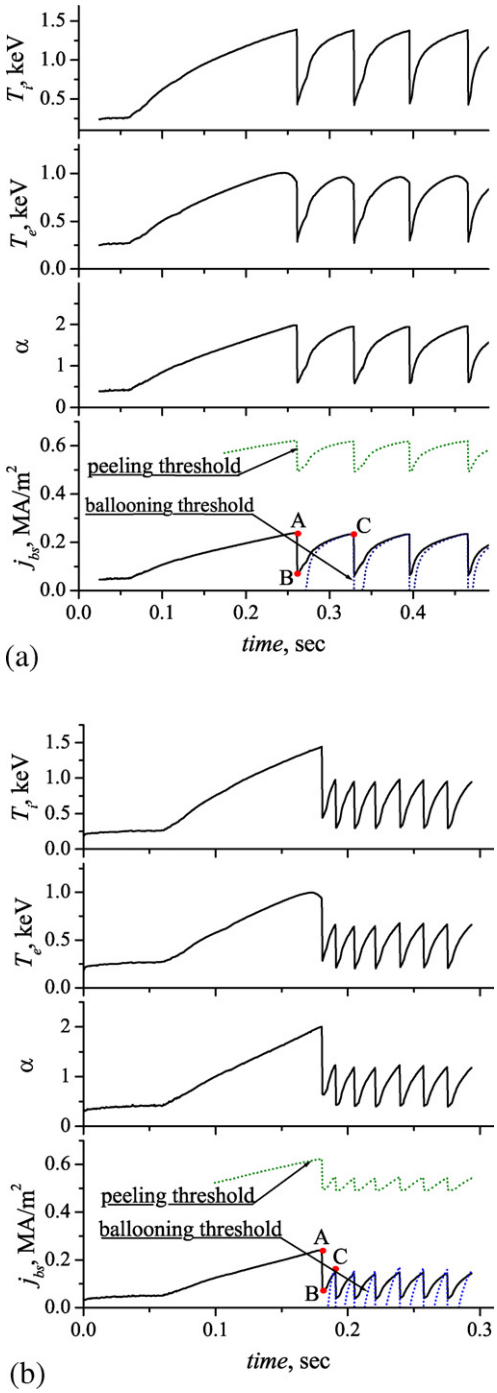

Figure 6. Time evolution of electron and ion temperatures, normalized pressure gradient and bootstrap current at 95% of the minor radius in the high triangularity discharge ($\delta = 0.6$) for the cases of (*a*) lower (6 MW) and (*b*) higher (8 MW) total auxiliary heating power. The range of bootstrap current that is stable for the peeling and ballooning instabilities is shown on the lower panels.

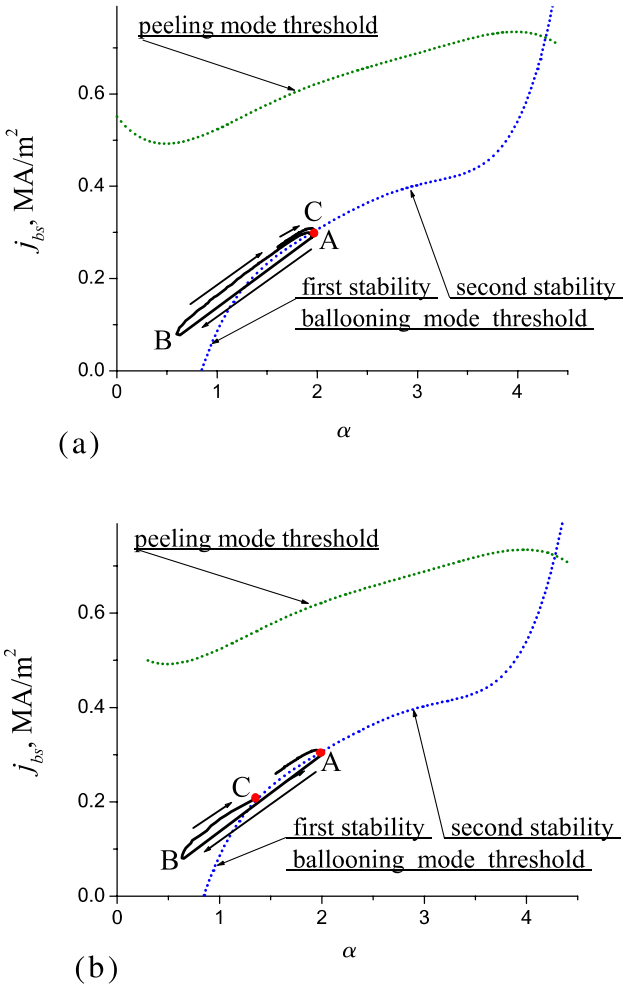

Figure 7. Peeling–ballooning stability diagrams with ELM cycles in the high triangularity discharge ($\delta = 0.6$) for the cases of (*a*) lower (6 MW) and (*b*) higher (8 MW) total auxiliary heating power. Points A and C represent two consecutive ELM crashes and correspond to point A and C on the lower panels in figure 6. Note that the normalized pressure gradient and bootstrap current on these diagrams are computed at the position of the maximum pressure gradient in the pedestal region, while the normalized pressure gradient and bootstrap current in figure 6 are computed at 95% of the minor radius.

are triggered by a ballooning instability in the second stability limit, while the discharges with high heating power (above 7 MW) are triggered by a ballooning instability in the first stability limit. In general, the pedestal pressure increases with heating power for type-1 ELMs. Experimental results [26–28] suggest that H-mode pedestal depends on the auxiliary heating power as

$$T_{\rm ped} \propto P_{\rm aux}^{\alpha},$$

where α ranges from 0.19 to 0.5. The experimental evidence is that α may vary over a wide range and depend sensitively on stability conditions and specific plasma parameters. The dependence of pedestal pressure on heating power may also reflect the type of ELM crash that is occurring. It is possible that the pedestal behaviour shown in figures 6 and 7 is the result of ELMs that are not type I ELMs.

5. Summary

An improved model is introduced for the H-mode pedestal and ELMs [8]. A parametrized peeling–ballooning stability criterion is implemented in the model, based on a detailed MHD stability analysis with the BALOO, DCON and ELITE

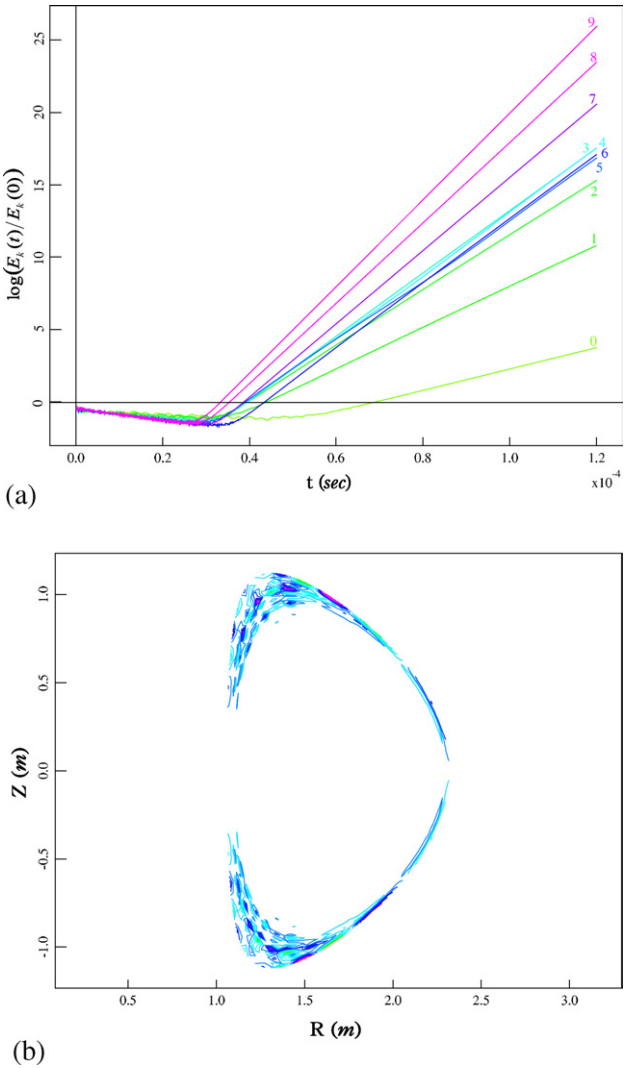

Figure 8. Results of the resistive MHD NIMROD code simulations for the first 10 toroidal mode numbers: (*a*) logarithm of the kinetic energy for different mode numbers; (*b*) contour plot of the eigen-functions.

codes. Two different scenarios for ELM crashes are shown. For the scenario with lower auxiliary heating power, ELMs are mostly caused by the ballooning instability in the second stability limit. For the scenario with higher auxiliary heating power (above 7 MW), ELMs might be caused by the ballooning instability in the first stability limit. Such ELM crashes are much less violent, because the pedestal pressure gradient does not build up as high before passing the stability condition and consequently they occur more frequently. In general, the frequency of ELMs increases with increasing auxiliary heating power (as shown in figure 5). The frequency of ELMs also depends on the plasma shaping. In particular, the dependence of ELM frequency on the triangularity is studied in this paper. It is found that higher triangularity discharges have a larger stability region than lower triangularity discharges (compare figures 3(*a*) and (*b*)). This observation is consistent with other MHD stability analyses [23] and with the conclusion that higher triangularity discharges can more easily access the second ballooning stability limit region of parameter space [6]. As a result, ELMs in lower triangularity discharges are much more frequent than ELMs in higher triangularity discharges (as shown in figure 5).

In conclusion, it is clear that additional MHD stability studies are required. In this paper, ideal MHD stability codes are used, while resistivity and two-fluid effects are expected to be important. A preliminary study with the resistive MHD NIMROD [29] code is under way. Some of the results of these simulations are shown in figure 8. The equilibrium selected for the NIMROD simulation corresponds to a stable case that is close to the nose of the stability diagram in figure 3(*a*). It is shown in figure 8(*a*) that modes with low toroidal mode numbers ($n \leqslant 10$) are linearly unstable. The NIMROD code uses exactly the same equilibrium generated with the TOQ code. At the same time, the equilibrium is not extended into the vacuum region in the NIMROD code. (In the DCON code, the extension of the equilibrium into the vacuum region is carried out using the supplementary code VACUUM [30].) In order to be consistent, an equilibrium with settings that eliminate the vacuum region has been analysed with the DCON code. The DCON results show that the peeling mode is unstable for the low toroidal mode numbers shown in this case, which might be the case that is observed with the NIMROD code. The eigen-functions shown in figure 3(*b*) are very localized close to the separatrix, which might indicate the signature of a peeling instability. In order to verify the results obtained with the MHD ideal stability code, a robust vacuum code should be used together with the NIMROD code which will be done in future studies.

Acknowledgments

The authors thank Dr G. Pereverzev for the installation and support of the ASTRA code and Dr L.E. Zakharov for the installation and help with the ESC equilibrium module.

References

[1] Bateman G., Bandrés M.A., Onjun T. and Kritz A.H. 2003 *Phys. Plasmas* **10** 3614
[2] Kinsey J., Staebler G. and Waltz R. 2002 *Phys. Plasmas* **9** 1676
[3] Erba M., Aniel T., Basiuk V., Becoulet E. and Litaudon X. 1998 *Nucl. Fusion* **38** 1013
[4] Pacher G. *et al* 2004 *Plasma Phys. Control. Fusion* **46** A257
[5] Schneider R. *et al* 2004 *Comput. Phys. Commun.* **164** 9
[6] Onjun T. *et al* 2004 *Phys. Plasmas* **11** 3006
[7] Lönnroth J.-S. *et al* 2004 *Plasma Phys. Control. Fusion* **46** 1197
[8] Pankin A.Y. *et al* 2005 *Plasma Phys. Control. Fusion* **47** 483
[9] Connor J.W. 1998 *Plasma Phys. Control. Fusion* **40** 531
[10] Lao L.L. 2000 *Plasma Phys. Control. Fusion* **42** A51
[11] Miller R.L. and VanDam J.W. 1987 *Nucl. Fusion* **27** 2101
[12] Glasser A.H. and Chance M.S. 1997 *Bull. Am. Phys. Soc.* **42** 1848
[13] Wilson H.R., Snyder P.B., Miller R.L. and Huysmans G.T.A 2002 *Phys. Plasmas* **9** 1277
[14] Lao L.L. *et al* 1999 *Nucl. Fusion* **39** 1785
[15] Pereverzev G. and Yushmanov P.N. 2002 *ASTRA Automated System for Transport Analysis in a Tokamak, Tech. Rep. IPP* 5/98 (Max-Planck Institut fur Plasmaphysik)
[16] Bateman G., Kritz A.H., Kinsey J.E., Redd A.J. and Weiland J. 1998 *Phys. Plasmas* **5** 1793
[17] Horton W. *et al* 2000 *Phys. Plasmas* **7** 1494

[18] Houlberg W.A., Shaing K.C., Hirshman S.P. and Zarnstorff M.C. 1997 *Phys. Plasmas* **4** 3230
[19] Snyder P.B. *et al* 2002 *Phys. Plasmas* **9** 2037
[20] Osborne T. *et al* 1997 *Proc. 24th Eur. Conf. on Controlled Fusion and Plasma Physics (Berchtesgaden, 1997)* (Geneva: European Physical Society) vol 21A, p 1701
[21] Wilson H.R. *et al* 2000 *Nucl. Fusion* **40** 713
[22] Sauter O., Angioni C. and Lin-Liu Y.R. 1999 *Phys. Plasmas* **6** 2834
[23] Snyder P.B. *et al* 2004 *Nucl. Fusion* **44** 320
[24] Kritz A.H. *et al* 2003 *Proc. 30th Eur. Conf. on Controlled Fusion and Plasma Physics (St. Petersburg, 2003)* (Geneva: European Physical Society)
[25] Murakami M. *et al* 2000 *Nucl. Fusion* **40** 1257
[26] Cordey J.G. *et al* 2003 *Nucl. Fusion* **43** 670
[27] Thomsen K. *et al* 2002 *Plasma Phys. Control. Fusion* **44**
[28] Mossessian D.A. *et al* 2003 *Phys. Plasmas* **10** 689
[29] Sovinec C.R. *et al* 2004 *J. Comput. Phys.* **195** 355
[30] Chance M.S. 1997 *Phys. Plasma* **4** 2161